Exp Fluids (2014) 55:1661
DOI 10.1007/s00348-013-1661-9

RESEARCH ARTICLE

Comparison of unsteady pressure fields on turrets with different surface features using pressure-sensitive paint

Stanislav Gordeyev · Nicholas De Lucca · Eric J. Jumper · Kyle Hird · Thomas J. Juliano · James W. Gregory · James Thordahl · Donald J. Wittich III

Received: 12 September 2013 / Revised: 10 December 2013 / Accepted: 21 December 2013

Abstract Spatially temporally resolved unsteady pressure fields on a surface of a hemisphere-on-cylinder turret with either a flat or a conformal window with realistic features such as gaps and "smile" cutouts were characterized using fast-response pressure-sensitive paint at $M = 0.33$ for several window viewing angles. Various statistical properties of pressure fields were computed, and geometry effects on the unsteady pressure fields were analyzed and discussed. Proper orthogonal decomposition was also used to extract dominant pressure modes and corresponding temporal coefficients and to analyze and compare instantaneous pressure structures for different turret geometric features and the window viewing angles. An unsteady separation off the turret and a recirculation region downstream of the turret were identified as dominant sources of the unsteady pressure. It was found that while all geometric features affected the unsteady pressure field, the "smiles," positioned spanwise-symmetrically on both sides of the turret, were the leading cause of these changes, followed by the looking forward flat window. The gaps, the side- and the back-looking flat window introduced only small local changes.

S. Gordeyev (✉) · N. De Lucca · E. J. Jumper
University of Notre Dame, Notre Dame, IN 46545, USA
e-mail: sgordeye@nd.edu

K. Hird · T. J. Juliano · J. W. Gregory
The Ohio State University, Columbus, OH 43235, USA

J. Thordahl · D. J. Wittich III
Air Force Research Laboratory, Directed Energy Directorate, Kirtland AFB, NM 87117, USA

1 Introduction

A hemisphere-on-cylinder turret is a common geometry for either directed energy or free-space communication systems to maximize the potential field-of-regard. The turret geometry has been previously shown to feature a highly three-dimensional turbulent flow field (Gordeyev and Jumper 2010), shown schematically in Fig. 1. This three-dimensional turbulent flow field has the effect of limiting the effective field-of-regard of the turret, as turbulent regions of the compressible flow introduce aberrations in the incident laser beam (Gordeyev and Jumper 2010). The flow over the hemisphere-on-cylinder turret has been studied extensively in recent years. There has been a large parametric study of the aero-optical properties of this geometry in flight using the Airborne Aero-Optics Laboratory, AAOL (Jumper et al. 2013; De Lucca et al. 2013a; Porter et al. 2013). Additionally, a variety of CFD studies have been performed on the turret geometry (Morgan et al. 2011; Morgan and Visbal 2012a, b; Jelic et al. 2013). Finally, various flow control strategies have been studied on this geometry (Morgan and Visbal 2012; Vukasinovic et al. 2013; Gordeyev et al. 2010). There has also been substantial research into the difference in aero-optical performance between flat and conformal windows on turrets (Gordeyev and Jumper 2010; De Lucca et al. 2013a).

As the turret is not a rigid body, its elastic motion can introduce a jitter into optical components used to project a laser beam from the turret. From a practical perspective, a jitter of only a few microradians can force a beam to miss a distant target. One source of turret vibrations arises from unsteady surface pressure fluctuations and resultant local forces that are due to the turbulent flow features around the turret. The beam jitter related to these flow-induced vibrations is termed the aeromechanical jitter of the turret.

Published online: 05 January 2014

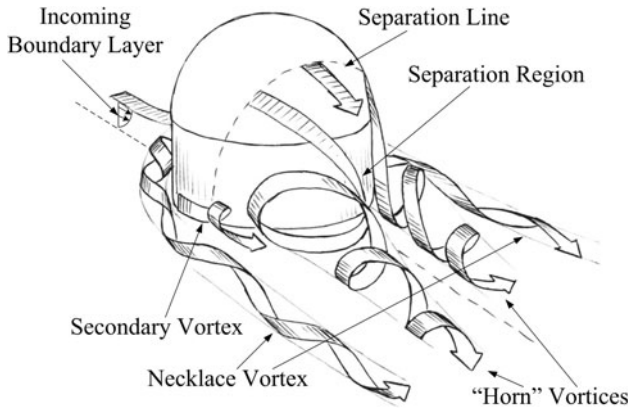

Fig. 1 Schematic of the flow around the hemisphere-on-cylinder turret (Gordeyev and Jumper 2010)

While the turret vibrational response depends on its internal structure, the unsteady pressure field depends only on the turret geometry and incoming Mach number. In addition, the unsteady pressure fluctuations on the surface of the turret are directly related to the turbulent structures, causing aero-optical global jitter and higher-order aberrations (De Lucca et al. 2012).

One way to investigate the time-changing pressure field on the surface of the turret is to use an array of unsteady pressure sensors, although in practice this usually gives a fairly coarse spatial resolution. Another alternative is to use a pressure-sensitive paint (PSP) (Liu and Sullivan 2005), where, by nature of the technique, a very detailed spatial resolution can be achieved. While the PSP technique has been known since the 1980s, its temporal response was very low, so results were limited to mostly steady-state pressure distributions. Recent advances in development of fast-response porous PSP coatings (Gregory et al. 2008) have allowed one to increase the frequency response of PSP up to several kilohertz (Gregory et al. 2014; Fang et al. 2012). Using a fast-response PSP, an unsteady pressure field around a hemispherical turret at transonic speeds, including dynamics of an unsteady shock on top of the turret, was investigated in Fang et al. (2012) and Fang et al. (2011).

This paper presents and analyzes experimental results obtained using the fast-response PSP to study the unsteady pressure fields on the surface of the turret with different realistic geometric features, such as a flat or a conformal window and cutouts near the base of the turret, at subsonic speeds. An extensive experimental database was constructed and analyzed by applying a proper orthogonal decomposition (POD), and dominant pressure modes and their temporal coefficients were extracted and are discussed here for different turret geometries and window viewing angles. A joint POD technique is also introduced and illustrated to provide a rigorous framework for comparing unsteady pressure fields for different geometries.

2 Experimental setup

The tested hemisphere-on-cylinder turret model, with a diameter $D = 30.5$ cm and a cylindrical base height $H = 11.1$ cm, shown in Fig. 2, was an exact replica of the AAOL turret shell used for aero-optical flight tests (Jumper et al. 2013). The turret has a rotating portion, or "donut," which allows it to continuously change the elevation angle of the window, and the whole turret assembly can be rotated to any azimuthal angle. The azimuth angle was measured clockwise from the upstream direction, when viewed from above, and the elevation angle was measured upward from the horizontal plane. The turret has several realistic features, such as 1-mm gaps between the rotating portion of the turret and trunnions, as well as cutouts, or "smiles," on both sides of the stationary portion of the turret, which are typically used to increase the field-of-regard at low elevation angles.

A complete description of the PSP tests is presented in Hird et al. (2013), so only essential details will be provided in this paper. A polymer-ceramic/PtTFPP paint with a frequency response up to at least 6 kHz was used (Gregory et al. 2008). The pressure-sensitive paint measurements were acquired in the White Field wind tunnel at the University of Notre Dame (see Fig. 3). The wind tunnel is a closed-return tunnel with a 0.9 m $\times$ 0.9 m test section and is capable of test section speeds up to a Mach number of 0.6. In this test, data were acquired at $M = 0.33$. The turret assembly allowed a continuous variation in both azimuthal and elevation angles. Additionally, the window could be switched between a flat window and a conformal one; the diameter of the flat portion of the window was 10.9 cm. Figure 4 presents a picture and a schematic of the layout of the experimental hardware. Three cameras, one on each side of the test section and one on the top, were used to capture the entire turret surface, allowing resolving the unsteady pressure field on the turret. The three cameras acquired frames at 2,000 Hz for 2.7385 s. Relevant details about each camera are given in Table 1. The turret was imaged twice using the high-speed cameras for wind-off and wind-on conditions, which is a characteristic procedure for PSP measurements. A total of 5,477 frames were taken by each camera with the eight UV LED arrays, four LED arrays on each side of the test section, illuminating the entire surface of the model.

Cameras 1 and 2 were monochromatic, and Camera 3 was color RGB. In order to capture different colors, Camera 3 utilized a Bayer arrangement of color filters on the pixel array of an image sensor, where each 2 $\times$ 2 cell

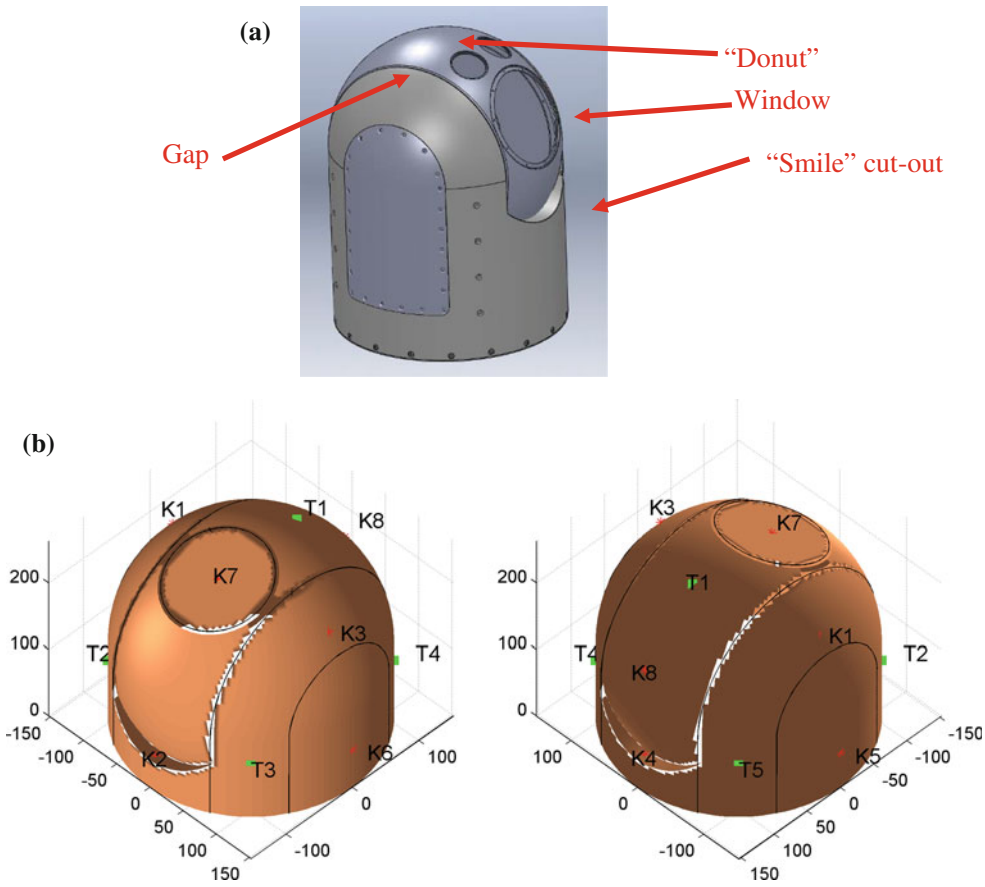

Fig. 2 **a** Turret model, **b** locations of pressure sensors *K1–K8* and thermoprobes, *T1–T5*, all dimensions are in millimeter

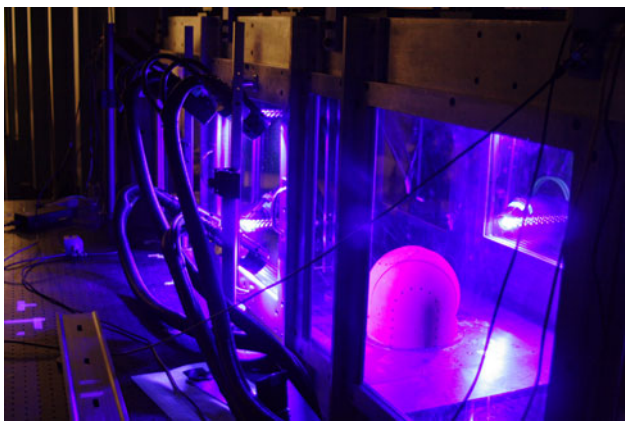

Fig. 3 Turret model in the test facility

contains two green, one blue and one red filter. As an unintended consequence, the color camera measured colors on staggered grids, resulting in one-half the spatial resolution of the monochromatic cameras. A second issue with the color camera was that a combination of the staggered color grid and filters reduced the overall intensity of the image, from 1,000 to 2,000 bits for the monochromatic camera down to 100–200 bits for the color camera. As image data are discrete both in space and in bit values, this decrease in the overall intensity of the image resulted in an increased discretization error, up to 4–7 % of the dynamic pressure, q, versus 0.7–1.5 % of q for the monochromatic cameras. A detailed error analysis will be presented later in the paper. In addition, Camera 3 measured the region at the front portion of the turret, where pressure fluctuations, measured by unsteady pressure sensors, were found to be approximately 1–2 % of the dynamic pressure. So, the combination of the much lower intensity and the lower spatial resolution of the images made data acquired by the color Camera 3 very noisy, with very small signal-to-noise ratios. After various attempts to reduce the noise present in images from Camera 3 by applying different filters, it was concluded that the signal-to-noise ratio was very low and data from Camera 3 were ultimately excluded from the present analysis.

Additionally, as shown in Fig. 2b, eight unsteady pressure Kulite sensors were used to verify the time variation of the PSP data and to provide a reference pressure for post-processing analysis. The pressure sensors were referenced to the interior pressure of the turret, which was measured with an external system. To complement the pressure sensors, five thermocouples were placed on the surface of the turret (see Fig. 2b) to account

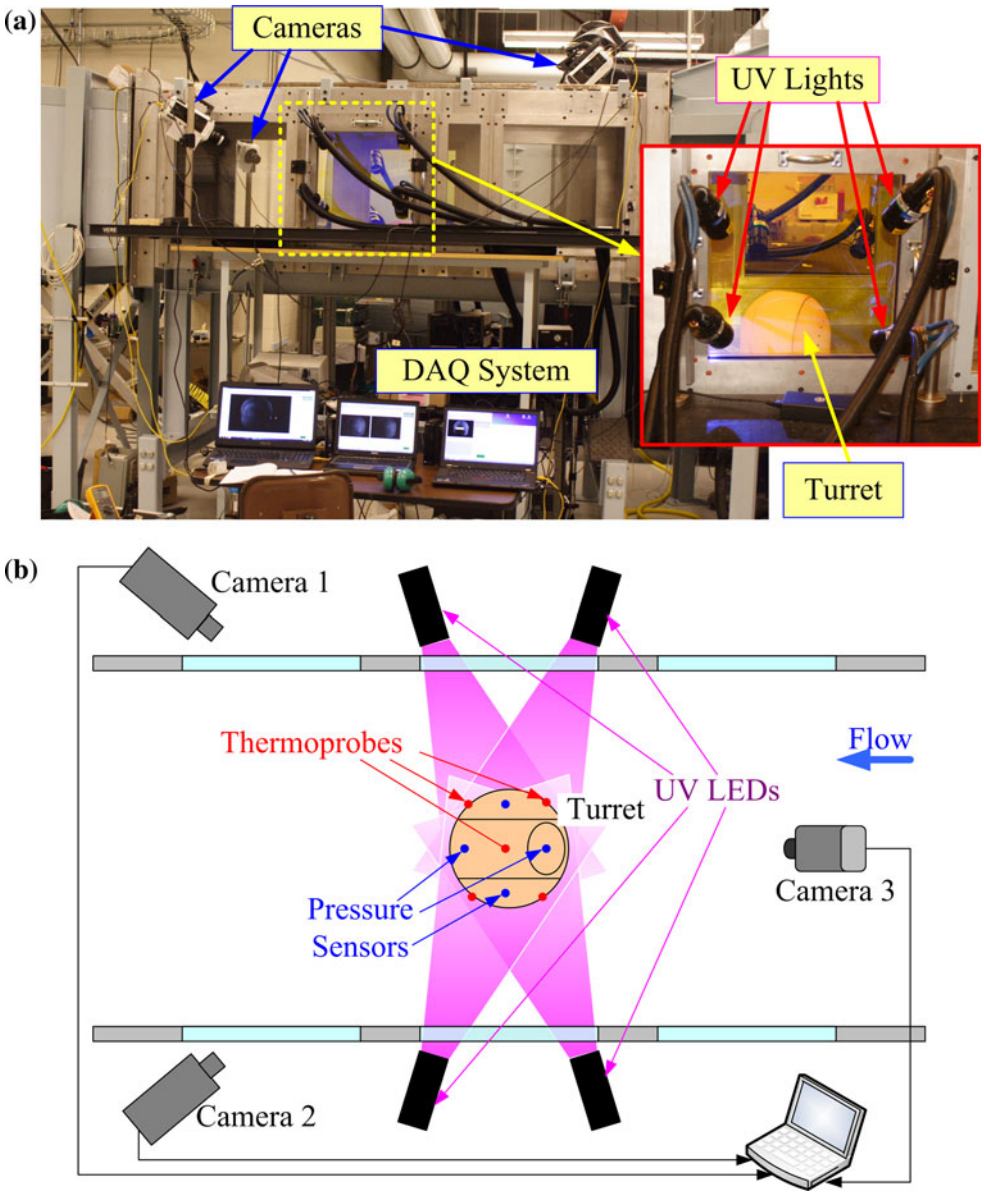

Fig. 4 Hardware configuration. **a** Picture and **b** schematic from the *top view* of wind tunnel. Flow goes from *right* to *left*

Table 1 Camera properties

Color space	Camera 1 Gray scale	Camera 2 Gray scale	Camera 3 RGB
Resolution	1,280 × 800	1,024 × 768	1,280 × 800
Frame limit	5,477	7,000	7,000
Frames/second	2,000	2,000	2,000

for any temperature variation between flow on/off conditions and any temperature gradients across the turret. The unsteady pressure and thermocouple data were acquired at 100 kHz for 10 s to provide better-resolved spectra over a larger frequency range. The pressure–temperature data acquisition system was triggered simultaneously with the cameras.

The turret geometric configurations tested are shown in Fig. 5. They include a test with a flat window (see Fig. 5a) and a test with a conformal window (see Fig. 5b). Additional tests were performed, in which the gaps surrounding the movable "donut" were covered with metal tape (see Fig. 5c) and, finally, both the gaps and the "smiles" were taped over, as shown in Fig. 5d, presenting the flow over a smooth surface rather than with various surface and surface slope discontinuities, caused by the presence of the gaps and the "smiles." Both the flat-window and the conformal-window turrets were tested at different azimuthal/elevation angles, indicated in Table 2.

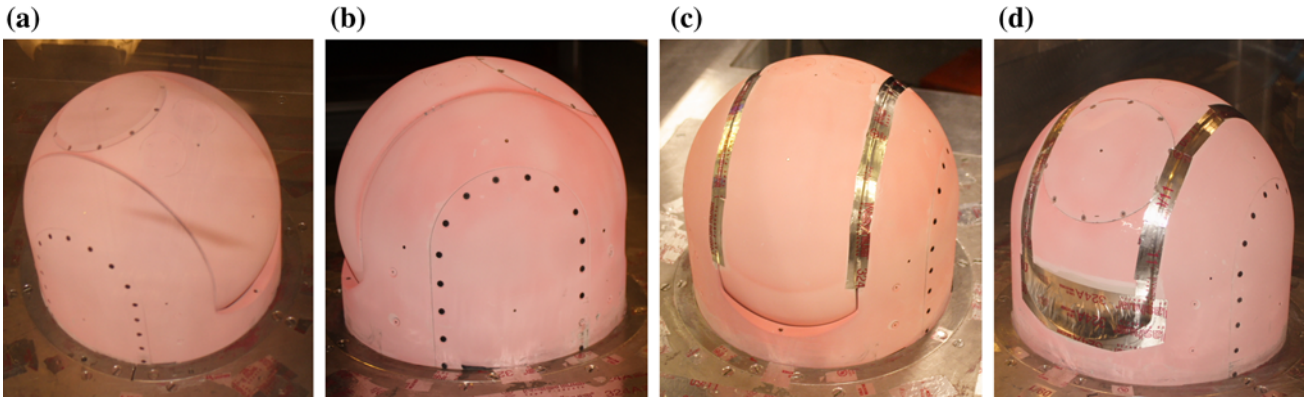

Fig. 5 Different turret geometries tested during PSP tests. **a** Turret with a flat window, **b** a conformal window, **c** a conformal window with gaps covered and **d** a conformal window with gaps and "smiles" covered

Table 2 Test matrix of turret positions

	Azimuth				
	0°	90°	125°	143°	180°
Elevation (°)					
45	×[a]	×			× (flat only)
60				×	
65		×			
69			×		

[a] For a conformal turret, included additional cases with gaps and "smiles" covered

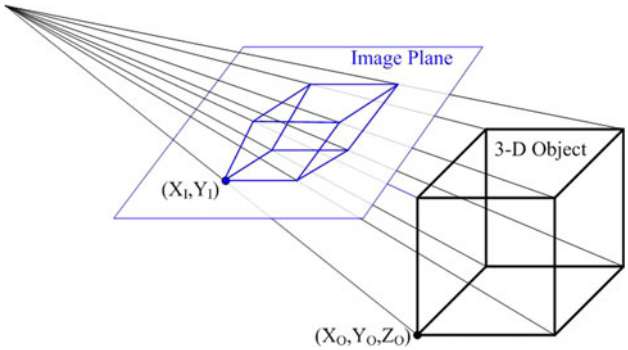

Fig. 6 Schematic of perspective projection

3 Data reduction

3.1 PSP calibration

A calibration was performed using a painted coupon placed in a pressure- and temperature-controlled calibration chamber. At a specified series of conditions, an image of the coupon was made, and the conditions and average intensity were recorded. Reference conditions were chosen to closely approximate those of the wind-off runs, and the pressure and intensity were normalized by these reference conditions. A surface fitting was used to provide a function returning a pressure ratio as a function of intensity ratio and instantaneous temperature.

This calibration was employed to extract instantaneous pressure fields from the registered images. The element-wise ratio of the flow-off mean to each flow-on frame was calculated, providing for each pixel a value of $I_{\text{ref}}/I_{\text{ref}}$. Preliminary testing explored the possibility of using the average of the registered flow-on frames as the reference condition, but it was found that the change in temperature made this inaccurate for a reference condition. The advantage of using the flow-on reference as a reference is that bulk pressure shifts are cancelled out, isolating the temporal variations. Thus, a two-step procedure was implemented, where the flow-on mean was referenced directly to the flow-off mean, providing a base pressure ratio, i.e., $P_{\text{ref}_{\text{on}}}/P_{\text{ref}_{\text{off}}}$. The quotient of the instantaneous pressure ratio and the average pressure ratio provides a more accurate value of $P/P_{\text{ref}_{\text{on}}}$. Pressure fields were normalized by the dynamic pressure, $q = 0.5\rho U_{\infty}^2$. A complete description of the calibration procedure is given in Jumper et al. (2013).

3.2 Surface pressure reconstruction from PSP tests

Knowing the exact location and orientation of each camera, relative to the turret, it is possible to map the pressure field from 2-D images onto the 3-D surface of the turret, using a perspective transformation matrix (PTM) technique (Carlbom and Paciorek 1978; Haralick 1980). The perspective projection is shown schematically in Fig. 6.

The perspective transformation allows us to compute $(X_{\text{I}}, Y_{\text{I}})$ location of the image point, if a 3-D coordinate of the object point $(X_{\text{O}}, Y_{\text{O}}, Z_{\text{O}})$ is given as

$$\begin{bmatrix} a \\ b \\ w \end{bmatrix} = \mathrm{PTM}^{*} \begin{bmatrix} X_{\mathrm{O}} \\ Y_{\mathrm{O}} \\ Z_{\mathrm{O}} \\ 1 \end{bmatrix}, \quad X_{\mathrm{I}} = a/w, \quad Y_{\mathrm{I}} = b/w,$$

where PTM is the 3×4 PTM, defined by the camera location and orientation angles. As accurate measurements of the camera orientation are difficult in practice, an alternative way to obtain a PTM is to take images of several non-coplanar points with known 3-D coordinates. After extracting 2-D locations of the points from the image, a PTM can be reconstructed using a least-square estimation (Tan et al. 1993). The advantage of this method is that it does not require explicit knowledge of the camera's location and orientation.

To accomplish this procedure, at the conclusion of the PSP tests the turret was replaced with a calibration mask, which consisted of a series of printed small dots at known locations. The mask was placed horizontally and then vertically, and images of the mask were recorded by all

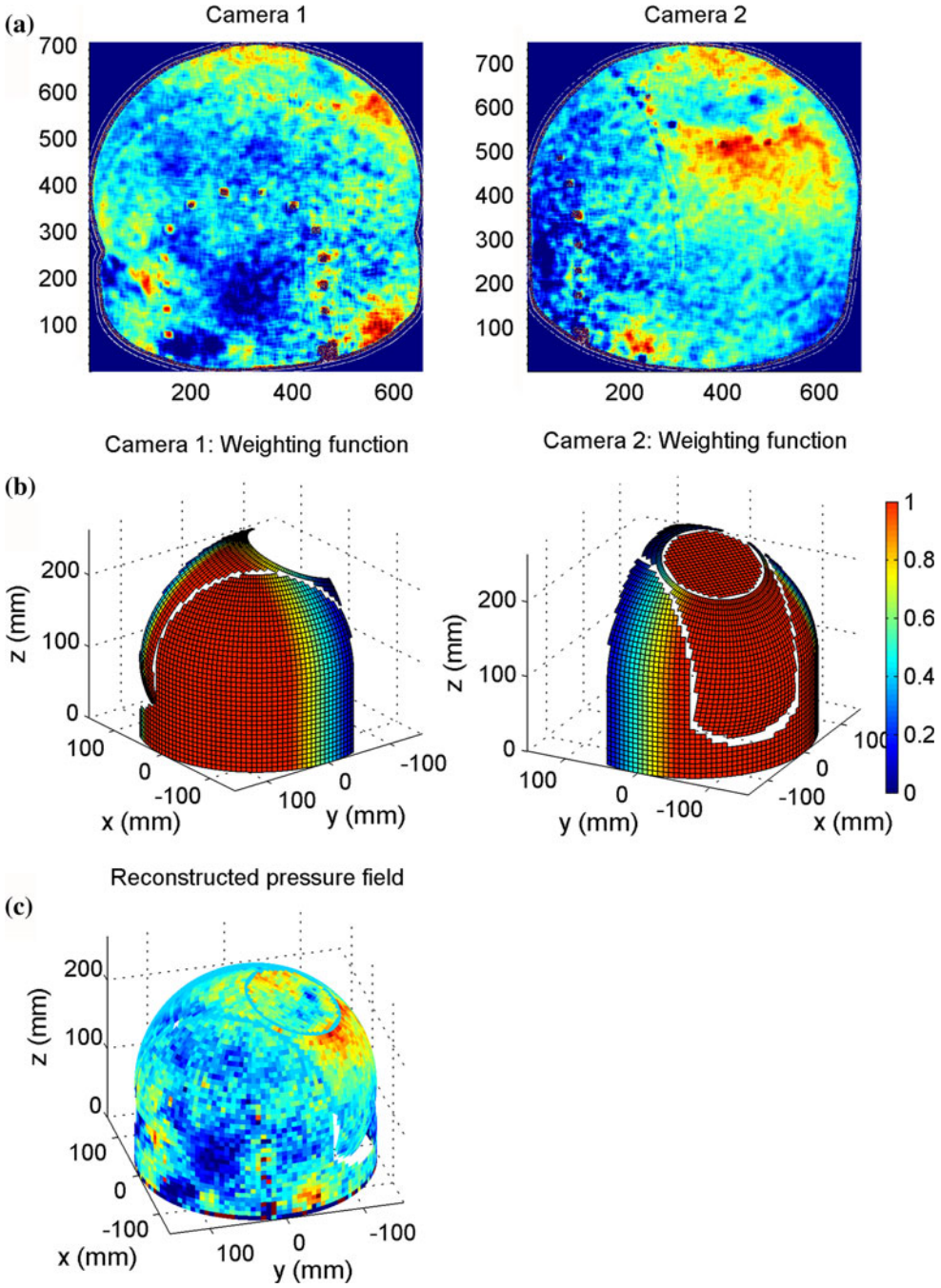

Fig. 7 **a** Individual frames from cameras, **b** corresponding weighting functions and **c** a reconstructed instantaneous pressure field on the surface of the turret. Flow goes along *x*-axis from positive to negative values

cameras. After extracting 2-D locations of the dots from images, a PTM was calculated for each camera.

The downstream portion of the entire turret surface between the azimuthal angle of 70° and 290° was approximated by a numerical grid with a grid step of 2.5° in both the azimuthal and the elevation angle directions, with a total number of grid points of approximately 4,500 points. Then, the turret surface was split into two regions by defining weighting functions, shown in Fig. 7b, to provide a unique mapping between the turret surface and the corresponding cameras' images. Using a PTM for each camera, for every grid point on the surface of turret, a corresponding image point was calculated, and applying a 10 × 10 Wiener filter centered at the image point, an instantaneous pressure value at that point on the turret was found. After instantaneous pressure values at every grid point on the surface of the turret in each region were computed, the full surface pressure field was reconstructed, using the weighting functions, shown in Fig. 7b, to "blend" data from different cameras. An example of a final 3-D reconstruction is shown in Fig. 7c, where individual 2-D pressure fields from Cameras 1 and 2, shown in Fig. 7a, were projected onto the 3-D turret surface.

An analysis of the wind-off or no-flow images provided an estimate of the error associated with measuring pressure using PSP. The noise was found to be approximately 2 % of the reference pressure, and after applying the 10 × 10 Wiener filter, the noise was reduced to 0.2 % of the reference pressure. The dynamic pressure was 0.07 of the reference pressure, so the overall error relative to the dynamic pressure was found to be 2.8 %. This is a conservative estimate, since, as it will be shown later in the paper, applying a cross-correlation-based POD technique to analyze the pressure data further reduces the error.

3.3 POD analysis

To provide a framework to analyze and compare the pressure fields for different turret geometric features and window viewing angles, a POD was used (Berkooz et al. 1993). From the spatially temporally resolved, mean-removed pressure field, $p(s, t)$, where s is a point of the turret surface, a time-averaged correlation matrix, $R(s,s') = \overline{p(s,t)p(s',t)}$, was calculated, where an overbar denotes time averaging. Using the correlation matrix, a set of spatial POD modes, $\phi_n(s)$, and corresponding eigenvalues or mode energies, λ_n, can be found by solving an integral equation using the direct method,

$$\int_S R(s,s')\varphi_n(s')\mathrm{d}s' = \lambda_n\varphi_n(s). \tag{1}$$

The solution of Eq. (1) gives a complete, orthogonal and fastest-converging set of POD modes. The instantaneous pressure field can be reconstructed using these modes as,

$$p(s,t) = \sum_n a_n(t)\varphi_n(s),$$
$$\text{where} \quad a_n(t) = \int_S p(s,t)\varphi_n(s)\mathrm{d}s, \quad \overline{a_n(t)a_m(t)} = \lambda_n\delta_{nm}. \tag{2}$$

The fastest-converging property of the POD technique allows approximation of the instantaneous pressure field as a sum of the first N modes, $p(s,t) \approx \sum_n^N a_n(t)\varphi_n(s)$.

Equations (1) and (2) were discretized over the turret grid and numerically solved using Matlab for every measured angle and a geometry type. Also, the normalized mode energy, $\lambda_n \equiv \lambda_n / \sum_n \lambda_n$, and the normalized cumulative energy, $\sigma_m \equiv \sum_n^m \lambda_n / \sum_n \lambda_n$, were computed for each case.

Figure 8 presents both the normalized and cumulative energies for the (90, 45), flat-window case. Here and below, the viewing angle is given in parenthesis with the azimuthal angle as the first number and the elevation angle as the second number. The full POD set for this case had 4,651 modes, but the first POD mode contained almost 30 % of the total energy of the pressure fluctuations, the first 10 modes had more than 60 % of the energy, the first 100 modes held more than 80 % of the total pressure-fluctuating energy, and the first 3,000 modes captured virtually all pressure "energy" of the flow.

To further illustrate the converging property of the POD set, the pressure field for the same case at a given moment was reconstructed using the first 10, 100 and 1,000 POD modes, and results are presented in Fig. 9. The original pressure field is also presented in Fig. 9a. As few as ten

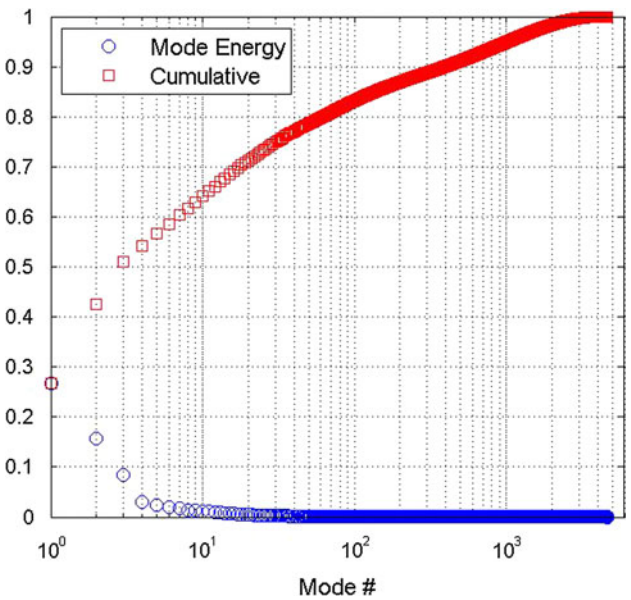

Fig. 8 The normalized and cumulative mode energies for (90, 45)-flat case

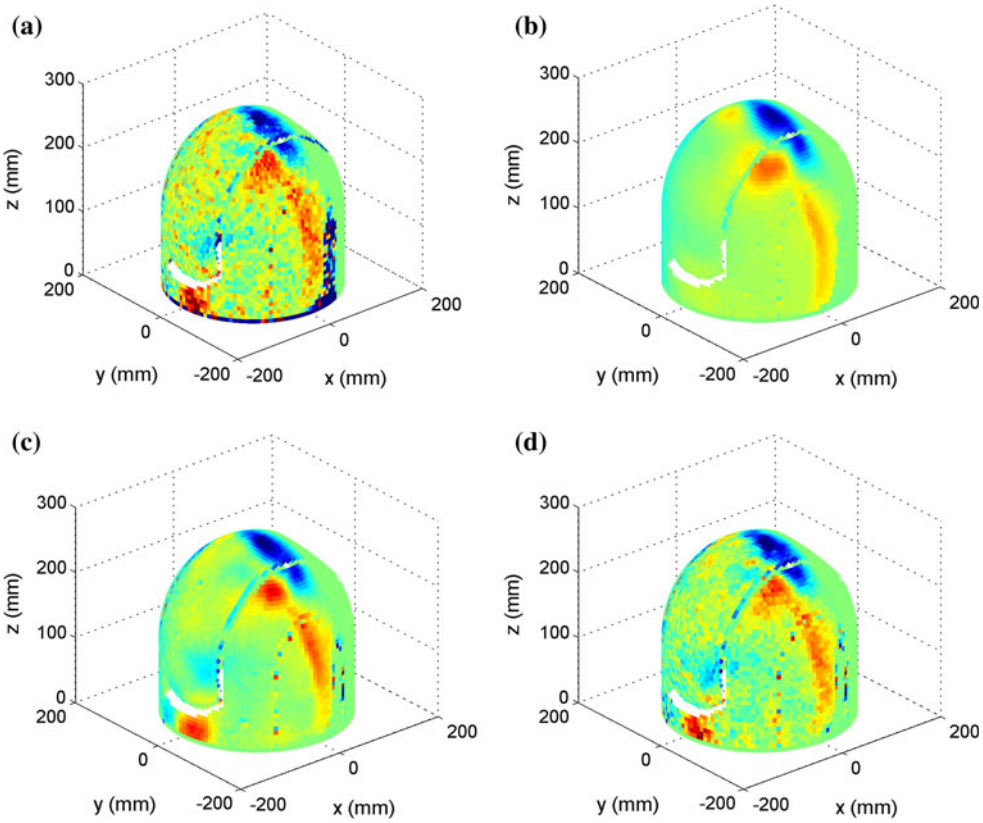

Fig. 9 **a** The representative instantaneous pressure field and POD reconstruction using **b** the first 10, **c** 100 and **d** 1,000 POD modes (0, 45), flat-window case, the flow goes along *x*-axis from *positive* to *negative* values

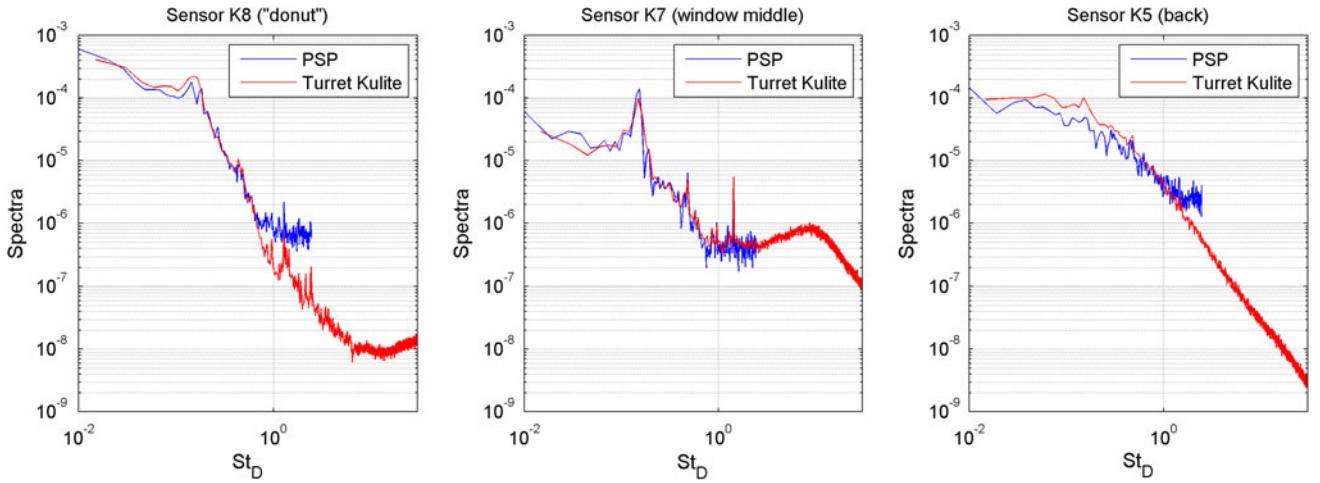

Fig. 10 Pressure amplitude spectra from unsteady pressure sensors (Kulites) and PSP for three different locations for the (90, 45), flat-window turret

POD modes (Fig. 9b) were able to capture most of the essential pressure features, and all of the features were properly recovered using 100 modes (Fig. 9c). The addition of more modes (Fig. 9d) simply added more noise to the pressure field, as the POD technique arranges modes by amount of cross-correlation or "order," so mostly incoherent noise was present in the very high-order modes. Thus, the POD technique, in addition to providing an optimal framework to investigate the flow, also presents an efficient way to further remove the noise present in the experimental data, while preserving the structures' features. After analyzing all cases, it was decided to keep only the first $N = 100$ modes in the POD-based pressure reconstruction for the remainder of the paper.

4 Results

4.1 Comparison between PSP and unsteady pressure sensors

Figure 10 presents a comparison between pressure spectra from unsteady pressure sensors and pressures extracted from PSP tests at three different locations on the turret. The normalized frequency is defined as $St_D = fD/U_\infty$. There is a very good agreement in both magnitude and frequency content between the pressure spectra, except for the very end of the PSP spectrum, where PSP spectra leveled off due to bit resolution errors and possibly an insufficient sampling rate. Overall, using the PSP technique, the pressure field over the turret surface was properly resolved in both time and space.

4.2 Effect of window geometry and positions of the "smiles"

Maps of time-averaged spatial $p_{rms}(s)$ for different azimuthal/elevation angles for the conformal-window turret are presented in Fig. 11. A dark blue color at the front portion of the turret in Fig. 11 and in Figs. 14 and 23 corresponds to the no-data region corresponding to Camera 3; in these plots, no data were replaced with zeros for illustrative purposes only and were not included in the POD analysis. The moving flow separation off the turret's backward surface caused significant temporal pressure fluctuations just upstream of the separation line, labeled in Fig. 11. Another region of increased pressure fluctuations was near the bottom of the downstream portion of the turret; this increase was due to an unsteady stagnation region caused by the recirculating flow region downstream of the turret, as well as a pair of "horn" vortices, located on both sides of the stagnation region (see Fig. 1).

Clearly, the spatial intensity of the pressure fluctuations depended on the location of the gaps and the "smiles," relative to the flow direction. When the "smiles" were located at the front and at the aft of the turret, they did not significantly affect the flow around the turret (see Fig. 11a). This configuration, as will be shown later, can be considered as a "baseline," hemisphere-on-cylinder-only configuration. The turret was next rotated by 90°, so the "smiles" were positioned spanwise-symmetrically on both sides of the turret. Slope discontinuities around the "smiles," particularly upstream vertical back-step portions, tripped the flow, so the flow separated prematurely on both sides of the turret and created strong vortical structures, clearly visible in representative instantaneous pressure fields in Fig. 12; these structures, through an interaction with the main separated region, significantly increased the pressure fluctuations near the bottom of the turret (see Fig. 11b). Finally, when the "smiles" were positioned non-symmetrically in the spanwise direction for the (125, 69)-case, they introduced spanwise-asymmetric spatial pressure fluctuations (see Fig. 11c). Inspection of representative instantaneous pressure fields, shown in Fig. 13, revealed that at this viewing angle the upstream "smile" created strong vortical structures, while no significant structures were formed by the downstream "smile." Also, the vortical structures were located closer to the mounting wall, compared with the azimuthal angle of 90° (see Fig. 12), suggesting that the curved, cavity-like portion of the "smile" was primarily responsible for creating vortical structures for the (125, 69)-case. Thus, a relatively small change of the azimuthal location of the "smiles," from 90° to 125°, resulted in a fairly significant difference of the unsteady pressure features on the turret (compare Figs. 12 and 13); as a consequence, for example, these different flow features will result in different unsteady forcing acting on the turret.

The spatial distributions of the pressure fluctuations, $p_{rms}(s)$, for the same angles but for the flat-window turret are shown in Fig. 14. When the flat window was facing forward, the slope discontinuity around the window tripped the flow and created vortical structures that convected over the top of the turret, shown in representative instantaneous pressure fields in Fig. 15; they were responsible for an additional increase in pressure fluctuations on top of the turret (see Fig. 14a) compared to the conformal-window turret for the same viewing angle, shown in Fig. 11a. For side-looking angles of (90, 45) and (125, 69), see Fig. 14b, d, the presence of the flat window created only small deviations from the spatial pressure fluctuations for the conformal-window turret for the same angles, see Fig. 11b, c. Predictably, most of the changes occurred over the flat-window aperture, where it created a slightly different pressure gradient and locally changed the flow dynamics and topology. The most notable difference for the pressure field over the window was observed in the (125, 69) and (143, 60) cases, where a slow-moving, time-changing local vortex was observed at the bottom of the flat window, creating a local increase in the pressure fluctuations, labeled in Fig. 14d, e. Nevertheless, overall spatial distributions of temporal pressure fluctuations were found to be sensitive mostly to the positions of the "smiles," rather than to the window type or its location, except when the flat window was facing forward. When the turret was rotated to the azimuthal angle of 143°, the upstream "smile" was in the region of the strong favorable pressure gradient at the upstream portion of the turret, so the tripped-by-"smile" flow quickly reattached and the formation of the vortical structures on that side of the turret was greatly suppressed (see Fig. 14e and representative snapshots of the instantaneous pressure field in Fig. 16). At the azimuthal angle of 90°, moving the flat window up from the elevation angle of

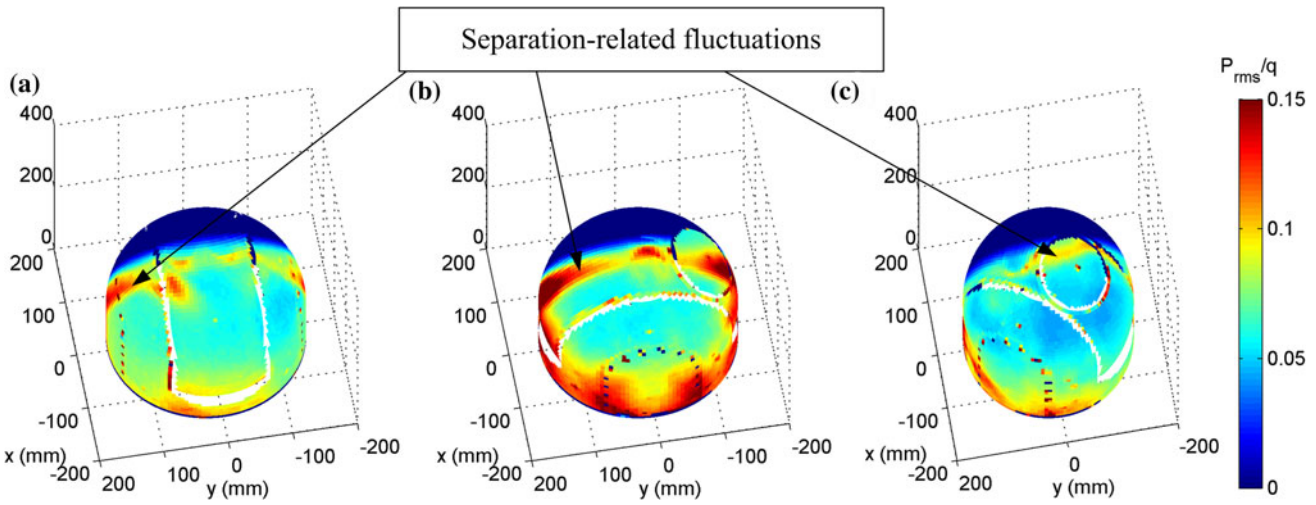

Fig. 11 Spatial distributions of $p_{rms}(s)$ for the conformal-window turret for the window azimuthal/elevation angles of **a** (0, 45), **b** (90, 45) and **c** (125, 69). The flow goes along *x*-axis from *positive* to *negative* values. Z-axis is not labeled for clarity

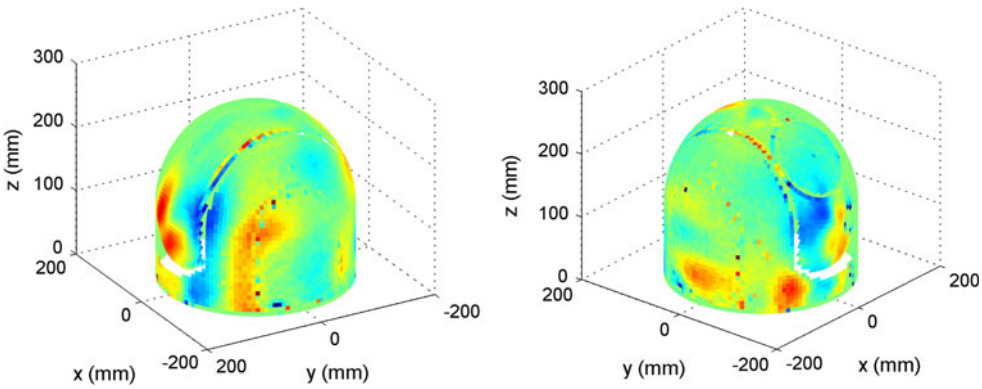

Fig. 12 Representative instantaneous pressure fields for (90, 45), conformal-window case. The flow goes along *x*-axis from *positive* to *negative* values

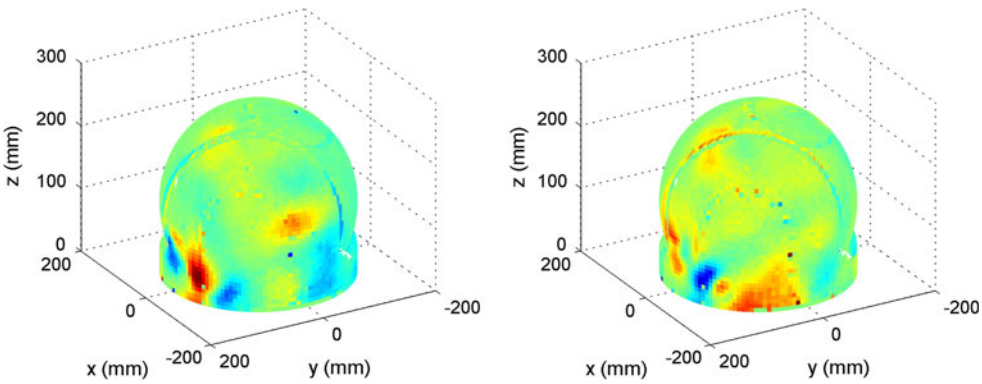

Fig. 13 Representative instantaneous pressure fields for the (125, 69), conformal-window case. The flow goes along *x*-axis from *positive* to *negative* values

45°–65° did not create any visible changes in the spatial p_{ms} distribution, compare Fig. 14b, c. When the flat window was positioned facing downstream inside of the separated flow region to the viewing angle of (180, 45) (see Fig. 14f), it did not introduce any significant differences in p_{rms} distribution, compare with Fig. 11a.

To further study the changes in the pressure fields for different locations of the turret geometric features, the POD modes and the corresponding temporal coefficients, as well as normalized and cumulative energies, were calculated for every case. The first five dominant modes for the (0, 45)-case for the conformal-window geometry (the "baseline"

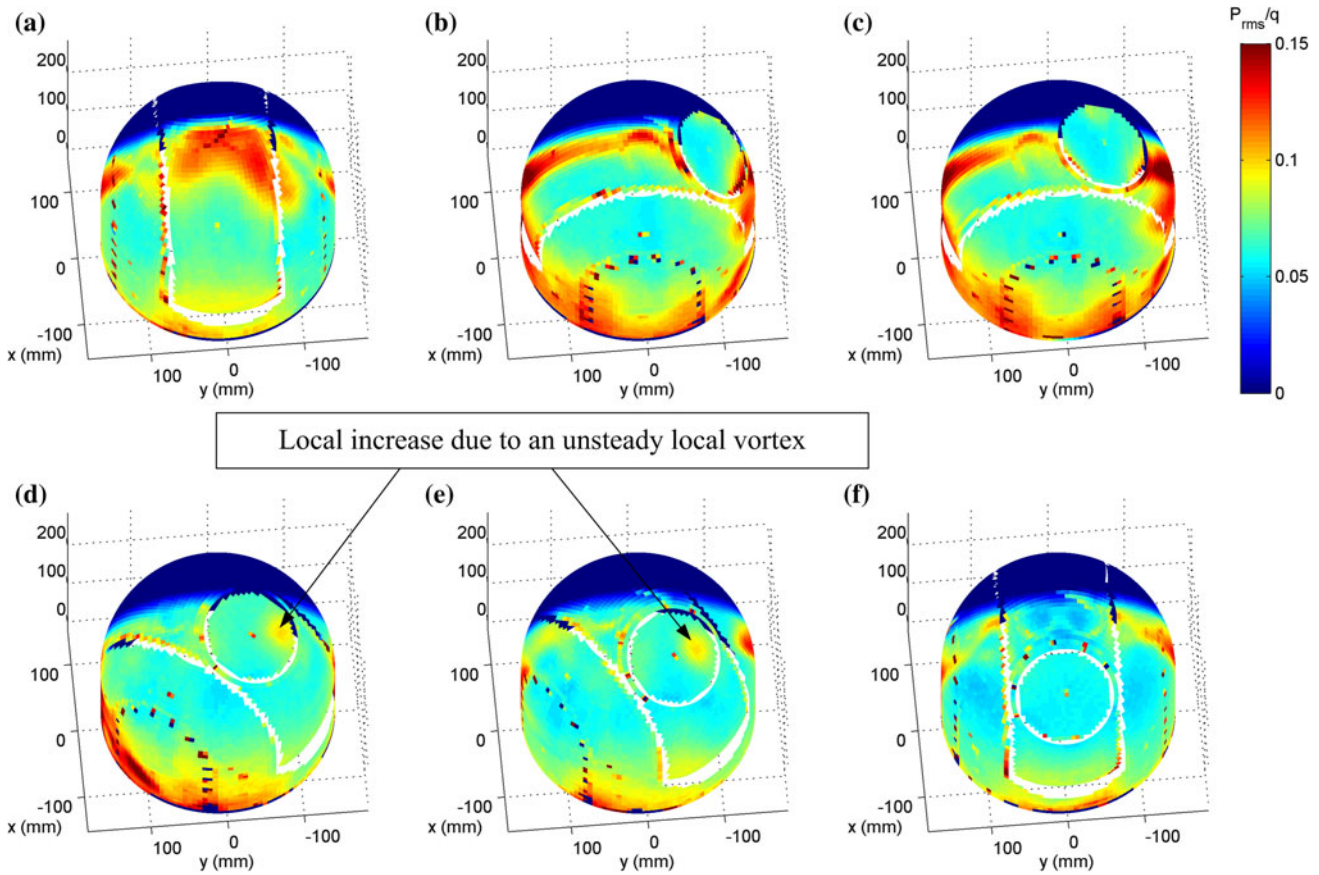

Fig. 14 Spatial distributions of $p_{\mathrm{rms}}(s)$ for the flat-window turret for the window azimuthal/elevation angles of **a** (0, 45), **b** (90, 45), **c** (90, 65), **d** (125, 69), **e** (143, 60) and **f** (180, 45). The flow goes along *x*-axis from *positive* to *negative* values. *Z*-axis is not labeled for clarity

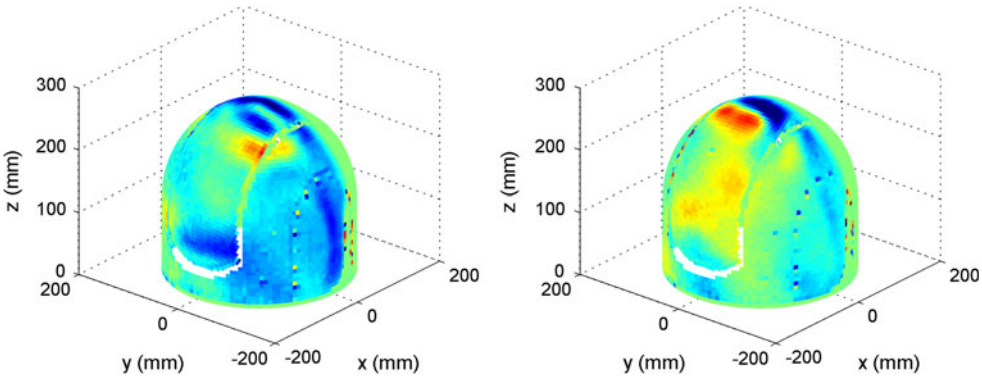

Fig. 15 Representative instantaneous pressure fields for the (0, 45), flat-window case. The flow goes along *x*-axis from *positive* to *negative* values

geometry) are presented in Fig. 17; the corresponding normalized and cumulative energies for each POD mode are given as a first and a second number in parenthesis on top of each plot and all other plots of the POD modes in this paper. For the conformal-window geometry, the first two POD modes had 26 and 20 % of the total pressure energy, and spatial distributions of these modes revealed that they corresponded to the separation-line-related pressure fluctuations, labeled in Fig. 11. Thus, the separation-related pressure fluctuations had a dominant contribution to the overall pressure fluctuation on the surface of the turret. These two modes appeared to be almost mirror images of each other relative to the vertical streamwise centerplane, and they had essentially nonzero values only at one side of the turret; as POD modes are statistically uncorrelated, this suggested that the separation-related pressure fluctuations on both sides of the turret were statistically independent. The third mode was related to the different region of the separation line located primarily on top of the turret; it appeared to be symmetric relative to the vertical

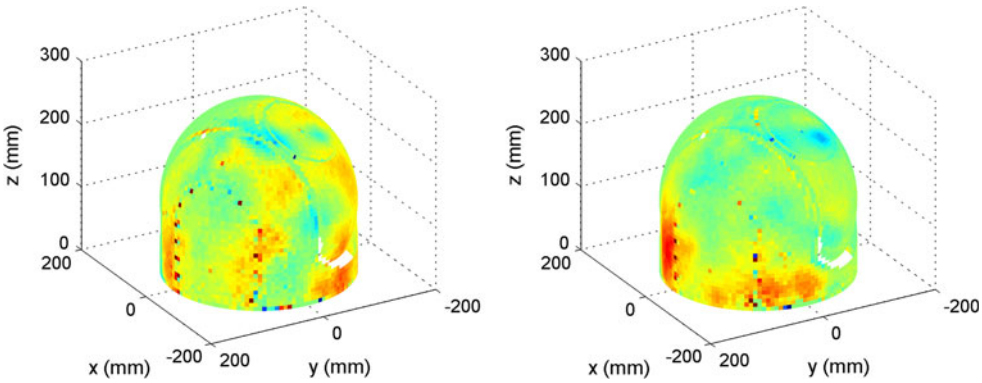

Fig. 16 Representative instantaneous pressure fields for the (143, 60), flat-window case. The flow goes along *x*-axis from *positive* to *negative* values

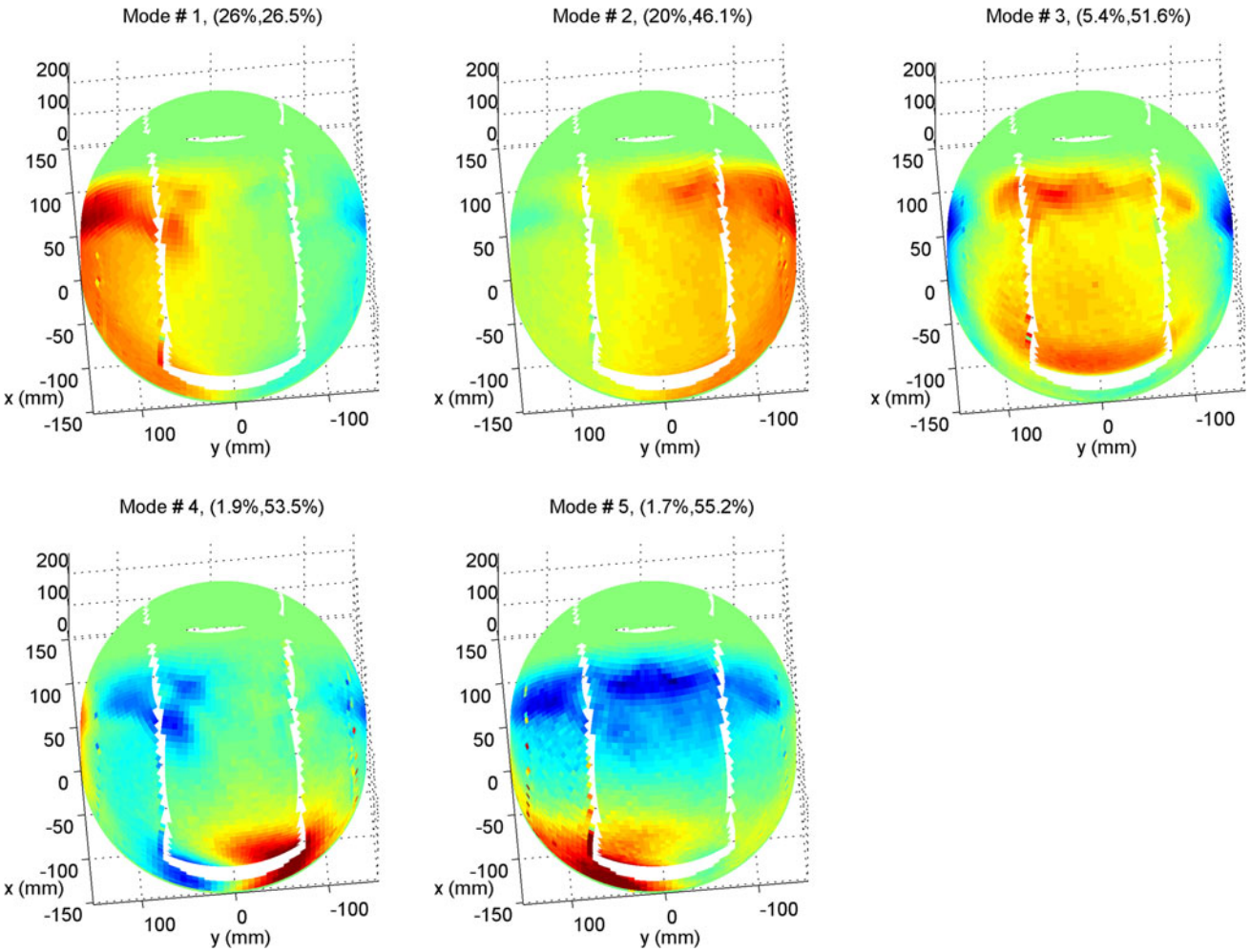

Fig. 17 First five POD modes for the (0, 45)-case for the conformal-window turret. The corresponding normalized and the cumulative energies for each POD mode are given as a first and a second number in parenthesis. The flow goes along *x*-axis from *positive* to *negative* values. *Z*-axis is not labeled for clarity

streamwise centerplane. Modes 4 and 5 were related to the unsteady stagnation region at the bottom of the turret, caused by the recirculating flow downstream of the turret. Analysis of higher modes revealed that they described additional details of the dynamics of the separation line and the stagnation region.

Five dominant POD modes for the same window viewing angle of (0, 45), but for the flat-window turret, are

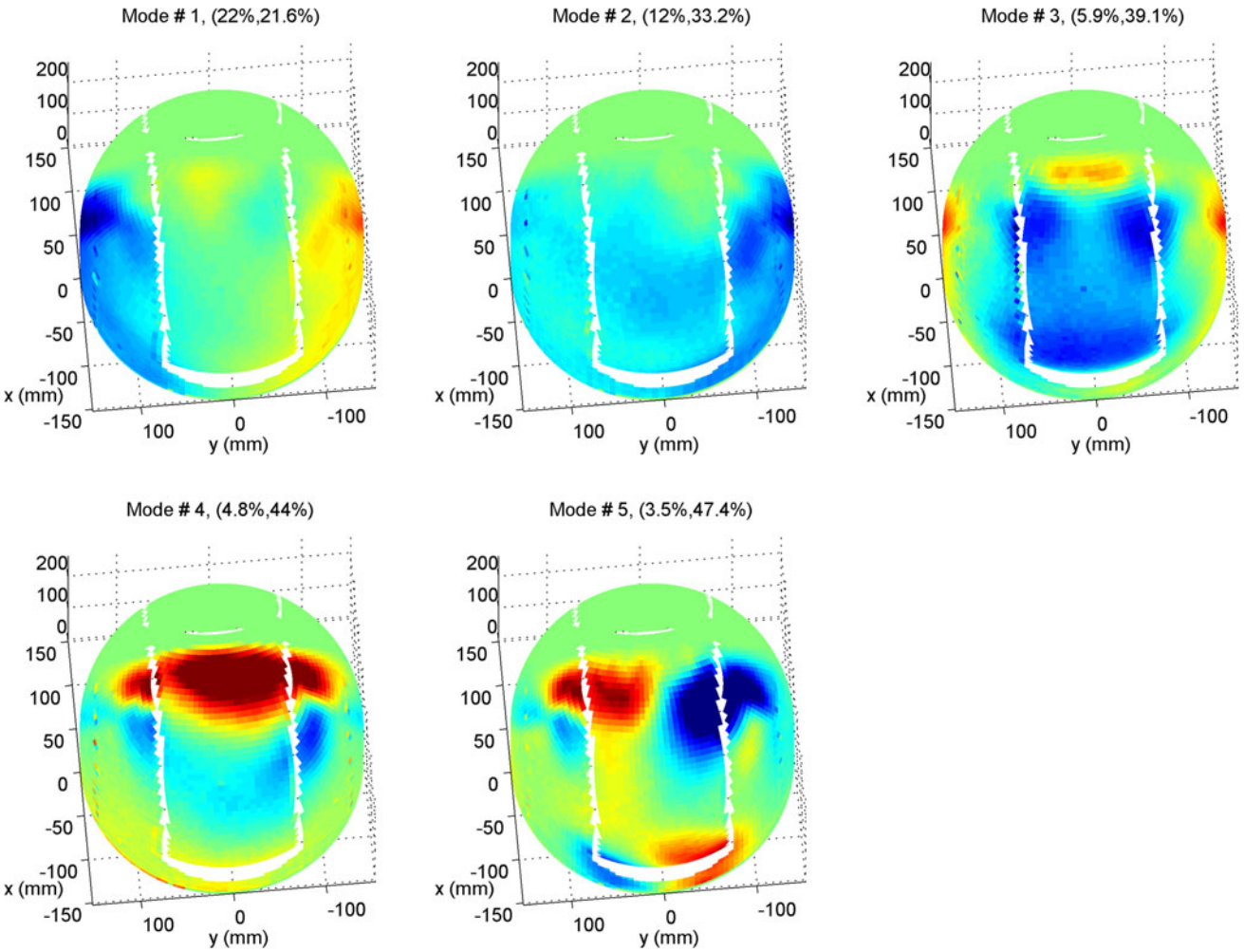

Fig. 18 First five POD modes for the (0, 45)-case for the flat-window turret. The corresponding normalized and the cumulative energies for each POD mode are given as a *first* and a *second number* in *parenthesis*. The flow goes along *x*-axis from *positive* to *negative* values. *Z*-axis is not labeled for clarity

presented in Fig. 18. The first two modes were similar in spatial distribution, as were the first two POD modes for the conformal-window turret, shown in Fig. 17. The only difference was for the region on top of the turret, where the separation was disturbed by the additional vortical structures created by the premature separation over the forward-facing flat-window aperture (see Figs. 14a and 15). Also, for the flat-window geometry, the first mode had only 22 % of the total energy and the second had only 12 % of the total energy. Mode 1 showed a stronger negative correlation between the separation-related pressure fluctuations on both sides of the turret, as it was antisymmetric, relative to the centerplane, compared with the conformal-window Mode 1, shown in Fig. 17. Thus, the presence of the forward-looking flat window increased the anticorrelation between pressure fluctuations on both sides of the turret, indicating changes in the global dynamics and topology of the separated turbulent region. Mode 2 in Fig. 18 shows the presence of a global spatial correlation on the downstream portion of the turret, related to the separation recirculation region. Modes 3–5 were related to the vortical structures convecting over the top of the flat-window turret. Overall, due to an increased interaction between the main separated region downstream of the turret and the additional vortical structures introduced locally by the flat window, the flow over the flat-window turret was less "organized," as it took the first six modes to capture 50 % of the total pressure energy, compared with the conformal-window turret, where 50 % of the energy were contained in the first three modes.

To understand the temporal dynamics of the dominant pressure structures, power spectra of the temporal coefficients of the dominant five POD modes for the conformal- and the flat-window turret are presented in Fig. 19a, b, respectively. For both window geometries, the first two modes had a peak around $St_D = 0.2$ and a smaller, sharper

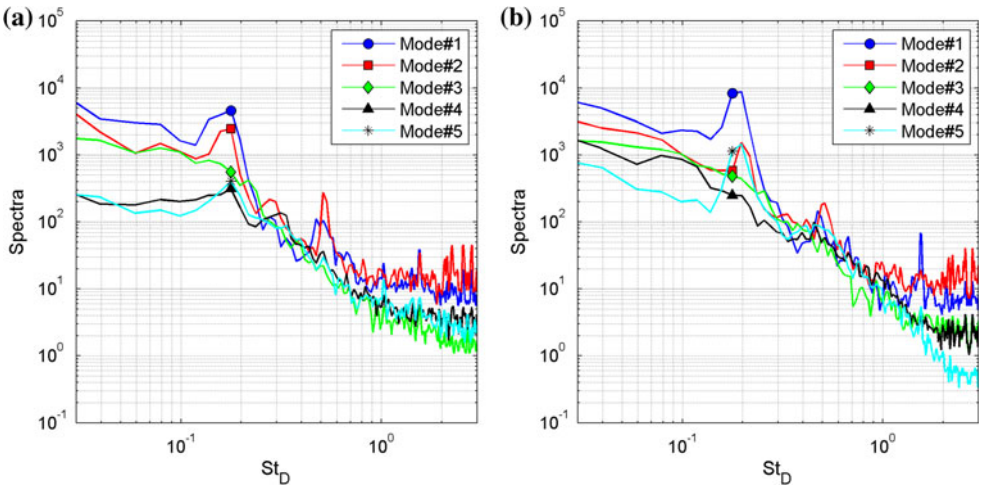

Fig. 19 Spectra for temporal coefficients for first five POD modes for the (0, 45)-case for **a** the conformal- and **b** flat-window turrets

peak around $St_D = 0.5$. The first peak was related to the unsteady flow separation over the turret; similar values of the unsteady-pressure spectral peak were observed in other unsteady pressure measurements on the downstream portion of the turret (Gordeyev et al. 2007; De Lucca et al. 2013b). The origin of the second peak was not quite clear and was possibly related to the blade-passing frequency of the tunnel-driving fan.

As it was shown in Figs. 11 and 12, when the turret was rotated to the azimuthal angle of 90°, and the "smiles" were positioned spanwise-symmetrically on each side of the turret, relative to the incoming flow, the "smiles" forced the premature flow separation on both sides of the turret and caused a significant increase in the pressure fluctuations downstream of the "smiles." As a consequence, the dominant four POD modes for the (90, 45), conformal-window case, shown in Fig. 20a, were significantly different from the POD modes for the conformal-window turret for (0, 45)-case, presented in Fig. 17. The first mode in Fig. 20a had a higher value of 33 % of the total pressure energy, and its spatial distribution was spanwise antisymmetric, compared with the first POD mode in Fig. 17. This suggested that in the presence of the spanwise-symmetric "smiles," the separation-related pressure fluctuations on both sides of the turret were strongly correlated and out-of-phase, indicating global changes in the separated region, compared with the "baseline" case, where the separation-related Mode 1 for the (0, 45), conformal-window case, Fig. 17, was largely spanwise-uncorrelated. Higher POD modes in Fig. 20a were found to be related to the unsteady stagnation region downstream of the turret.

When the conformal window was replaced with the flat one for the azimuthal angle of 90°, the side-facing flat window introduced a spanwise-asymmetry to the turret surface. Nevertheless, this change in the surface geometry introduced only local changes in the pressure field, primarily over the window itself, compare Figs. 11b and 14b. Therefore, the first four dominant POD modes for the flat-window (90, 45)-case, presented in Fig. 20b, were similar to the dominant POD modes for the conformal-window turret, shown in Fig. 20a, although not necessarily in a one-to-one comparison, as, for instance, Mode 3 for the conformal window was similar to Mode 4 for the flat window. This comparison also confirmed that the dominant sources for the increased pressure fluctuations at this viewing angle were the "smiles" and not the window type. Spectra of the temporal coefficients for the dominant POD modes were quite similar to the spectra for the (0, 45)-case, shown in Fig. 19, with a dominant peak around $St_D = 0.2$ and therefore are not presented here.

As the POD technique decomposes the pressure field as a sum of dynamical modes, the analysis of higher-order POD modes revealed additional details about less energetic, but still dynamically important, "smiles"-induced, traveling vortical structures observed for viewing angles of (90, 45) (see Fig. 12) and for the (125, 69)-case (shown in Fig. 13). Inspection of Modes 5–8 for the (90, 45)-case, presented in Fig. 21a, showed the averaged streamwise spacing of approximately 45° between positive and negative values in the POD modes downstream of the "smiles"; this is related to the average streamwise spacing between traveling structures. Also, the POD modes showed a significant extent of the traveling structures away from the mounting wall, up to more than half of the total turret height. In comparison, for the (125, 69)-case, shown in Fig. 21b, traveling structures were located closer to the wall, mostly on the cylindrical portion of the turret, with a very similar spacing between structures. Again, this analysis has shown that the details of the instantaneous pressure fields were sensitive to the relative position of the "smiles."

While the traveling vortical structure for the (90, 45) and (125, 69) cases had a well-defined spatial spacing between

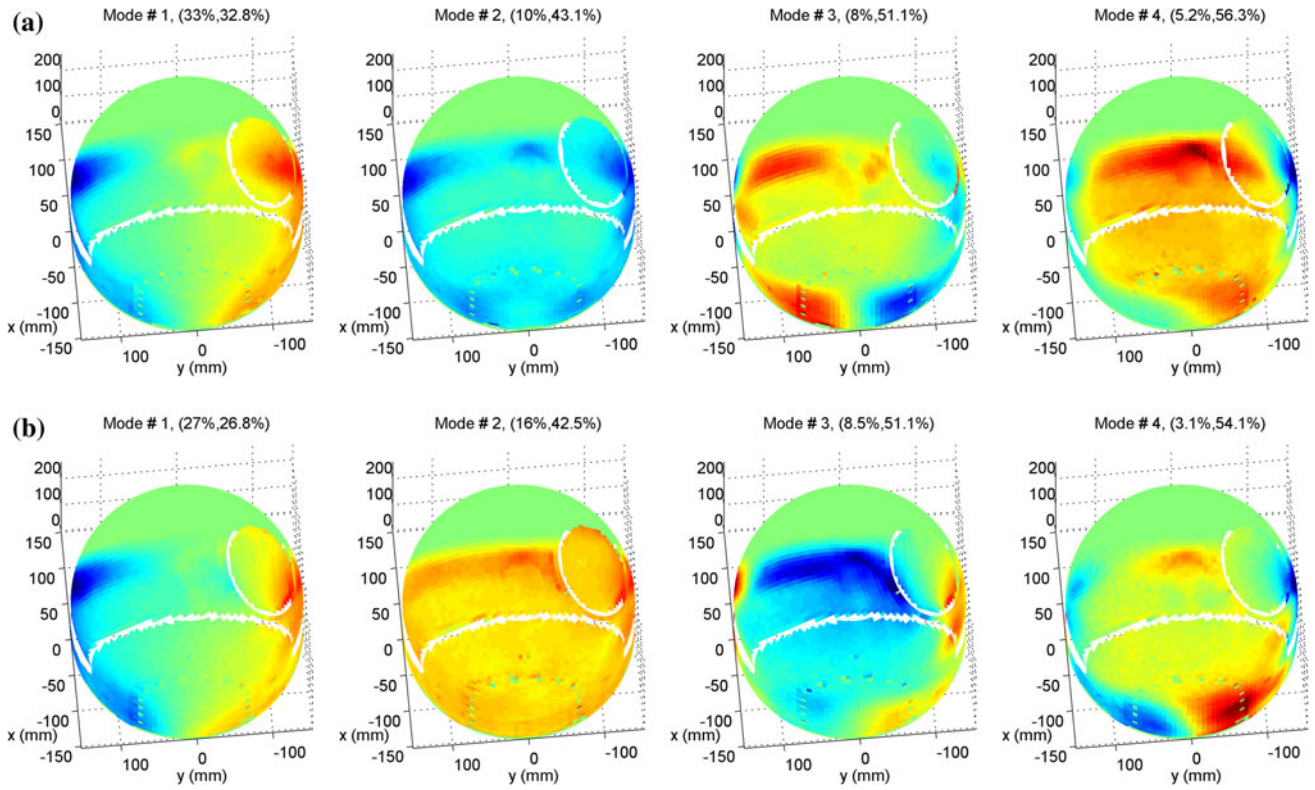

Fig. 20 First four POD modes for the (90, 45)-case for **a** the conformal- and **b** the flat-window turret. The corresponding normalized and the cumulative energies for each POD mode are given as a *first* and a *second number* in *parenthesis*. The flow goes along *x*-axis from *positive* to *negative* values. *Z*-axis is not labeled for clarity

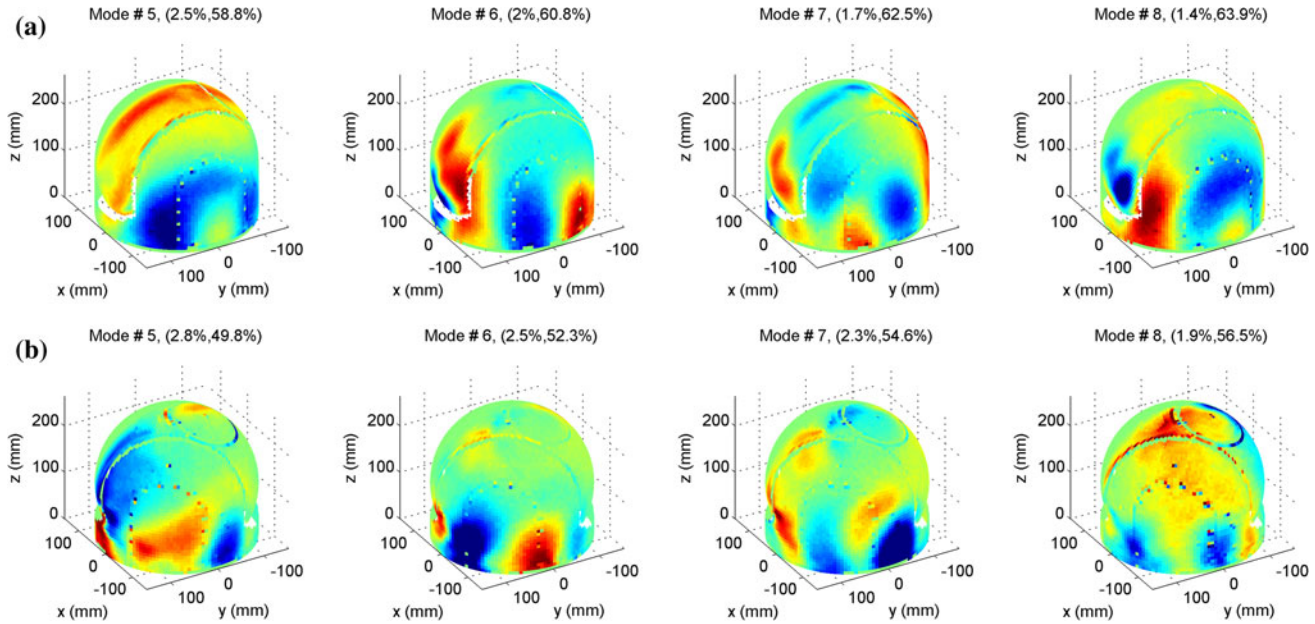

Fig. 21 POD modes 5–8 for the conformal turret for **a** the (90, 45)-case and for **b** the (125, 69)-case. The corresponding normalized and the cumulative energies for each POD mode are given as a *first* and a *second number* in *parenthesis*. The flow goes along *x*-axis from *positive* to *negative* values

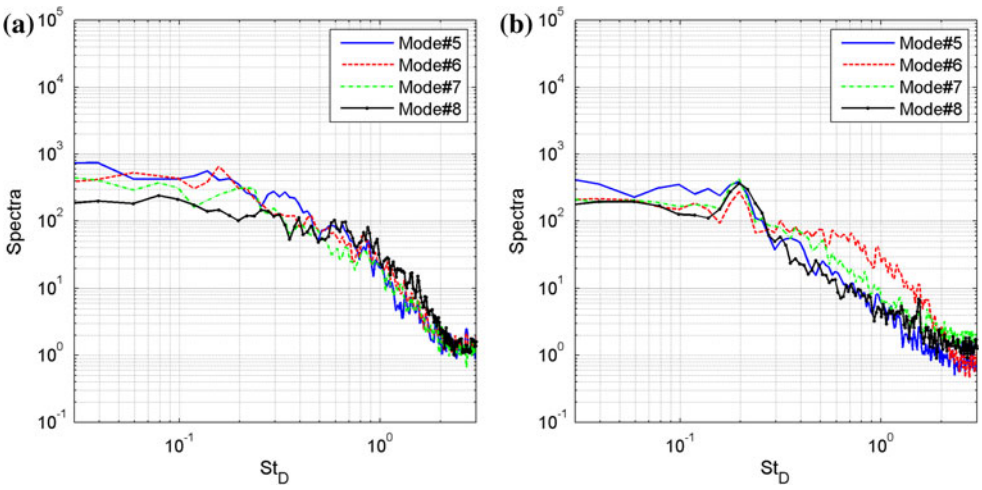

Fig. 22 Spectra for temporal coefficients for higher POD modes #*5–8* for **a** the (90, 45)-case and **b** for (125, 69)-case for the conformal-window turret

consecutive structures, the analysis of the spectra of temporal coefficients for Modes 5–8 for the (90, 45) and the (125, 69) cases, shown in Fig. 22, did not reveal any clear periodicity, except for a very small peak around $St_D = 0.2$. This observation, supported by the inspection of the temporal evolution of the instantaneous pressure fields, suggests that the vortical structures at these viewing angles were randomly shed off of the "smiles."

4.3 Effect of the presence of gaps and the "smiles"

The previous section has discussed the effect of the position of the "smiles" on the unsteady pressure field on the turret. By covering the gaps and the "smiles," one can directly study the "baseline" geometry and how the presence of these geometric features affects the pressure field. The time-averaged spatial distribution of the unsteady pressure field for the (0, 45), conformal-window case is presented in Fig. 23, with both the gaps and the "smiles" present (Fig. 23a), the gaps covered (Fig. 23b) and both the gaps and the "smiles" covered (Fig. 23c). For this azimuthal angle, the gaps were aligned with the incoming flow and air was forced to flow through the gaps due to pressure gradients on the surface of the turret. The flow through the gaps formed weak blowing jets on the downstream portion of the turret. The interaction of jets with the separated flow created additional vortical structures, which were responsible for a localized increase in p_{rms} values, marked in Fig. 23a. Representative instantaneous pressure fields for the gaps uncovered, highlighting these structures, are shown in Fig. 24. At this window viewing angle of (0, 45), the "smiles" were located either at the front or at the back of the turret and did not significantly disturb the flow. As a result, there was no visible difference between the covered-gaps geometry and the covered-gaps-and-smiles geometry (see Fig. 23b, c, respectively). Further, the presence of the gaps did not significantly modify the pressure spatial distribution on the turret either, so all three configurations can be considered as "baseline" geometry.

4.4 Joint POD analysis

While POD finds an optimal set of eigenmodes for every data set and it is useful to examine each POD set separately to understand the dynamics and the topology of the dominant structures, it gives a *different* set for every case, potentially complicating the comparison between the pressure dynamical structures for different cases, as discussed when comparing POD modes for the different windows in Fig. 20. In order to provide an alternative way to compare different cases to examine, for example, the effect of either the flat or the conformal window on the pressure field, one can combine data sets for different cases,

$$p_{\mathrm{Joint}}(s,t) = \{p(s,t,\mathrm{Param1}), p(s,t,\mathrm{Param2})\cdots\},$$

where Param$i$ is a viewing angle or the window type, for instance, and find a joint POD spatial set $\{\Lambda, \Phi(s)\}_n$ by solving the POD integral equation. It is easy to show that a corresponding joint correlation matrix is an average of all individual correlation matrices,

$$R_{\mathrm{Joint}}(s,s') \equiv \frac{1}{M}\sum_{\mathrm{All\ Param}}^{M} R(s,s';\mathrm{Param}).$$

This joint POD set, by construction, is the same for all cases. The difference between pressure fields for different parameters will be only in temporal coefficients and, consequently, in values of normalized and cumulative energies,

$$a_n(t;\mathrm{Param}) = \int_S p(s,t;\mathrm{Param})\Phi_n(s)\mathrm{d}s,$$
$$\Lambda_n(\mathrm{Param}) = \overline{a_n^2(t;\mathrm{Param})}.$$

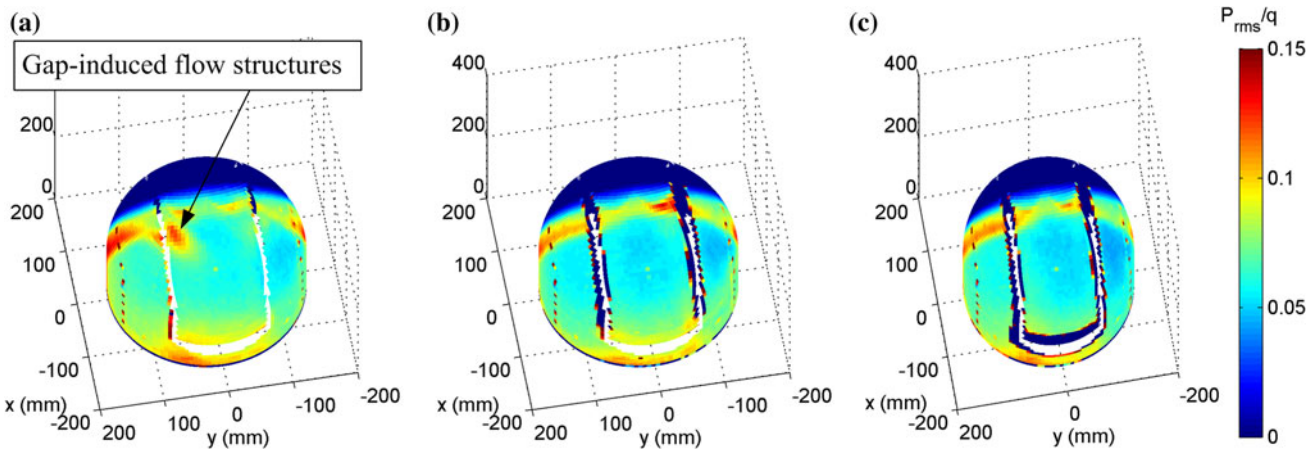

Fig. 23 Spatial distributions of $p_{rms}(s)$ for the conformal-window turret at (0, 45) for **a** gaps open, **b** gaps covered and **c** gaps and "smiles" covered. The flow goes along *x*-axis from *positive* to *negative* values. *Z*-axis is not labeled for clarity

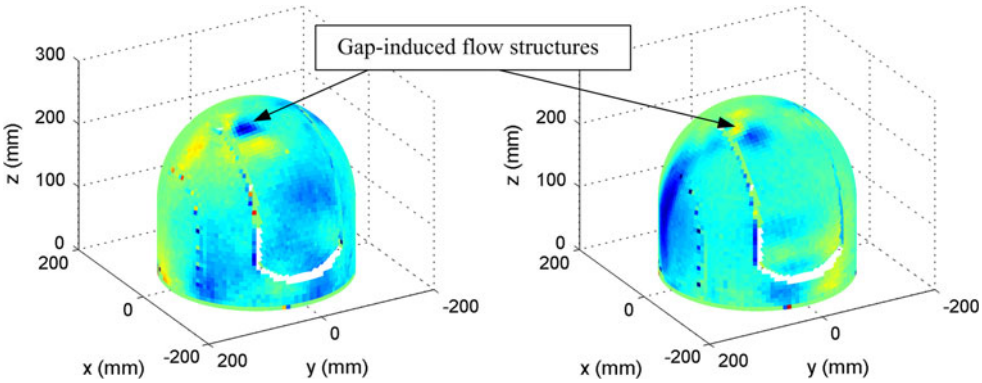

Fig. 24 Representative instantaneous pressure fields for the (0, 45), conformal-window case with the gaps and the "smiles" present. The flow goes along *x*-axis from *positive* to *negative* values

An example of the joint POD analysis for the (0, 45) viewing angle is shown in Fig. 25, where the first six joint POD modes are presented for a combined data set including both the conformal- and the flat-window cases. To compute these joint POD modes, instantaneous pressure fields for both cases were interpolated to the same grid, and the method of snapshots was used to compute the modes. As before, the first three dominant modes were related to the unsteady flow separation off the surface of the turret, and the other modes described the vortical structures formed by the slope discontinuity of forward-facing flat window. To study the contribution of each mode to the unsteady pressure field as a function of geometry, each joint POD mode was projected into the instantaneous pressure field corresponding to the conformal-window turret and, separately, to the flat-window turret to compute temporal coefficients. Time-averaged squares of the temporal coefficients of each joint mode for different geometries, which are relative energies of each mode, are presented in Fig. 26a, and the normalized cumulative energies *for each window geometry* are plotted in Fig. 26b. For the conformal-window turret, the first two joint POD modes were more energetic than for the flat-window turret, indicating that the flat-window-induced separation disrupted the overall separation over the turret. Modes 4–20 were more energetic for the flat-window turret, compared with the conformal-window turret, as these modes described the details of the flat-window-induced separation on top of the turret, and the conformal-window turret did not have this local separation. The first 100 joint POD modes described 80 % of the total pressure energy, very similar to the normalized cumulative energies for the first 100 POD modes from individual POD sets. Thus, the joint POD approach allows studying the relative contribution of each joint POD mode to the pressure dynamics for that particular turret geometry. Similarly, the approach can be used to study the relative importance of each joint POD mode as a function of the position of the "smiles" by combining data sets for different viewing angles.

5 Conclusion and discussion

A fast-response pressure-sensitive paint technique with multiple high-speed cameras was used to experimentally extract spatially and temporally resolved pressure fields for

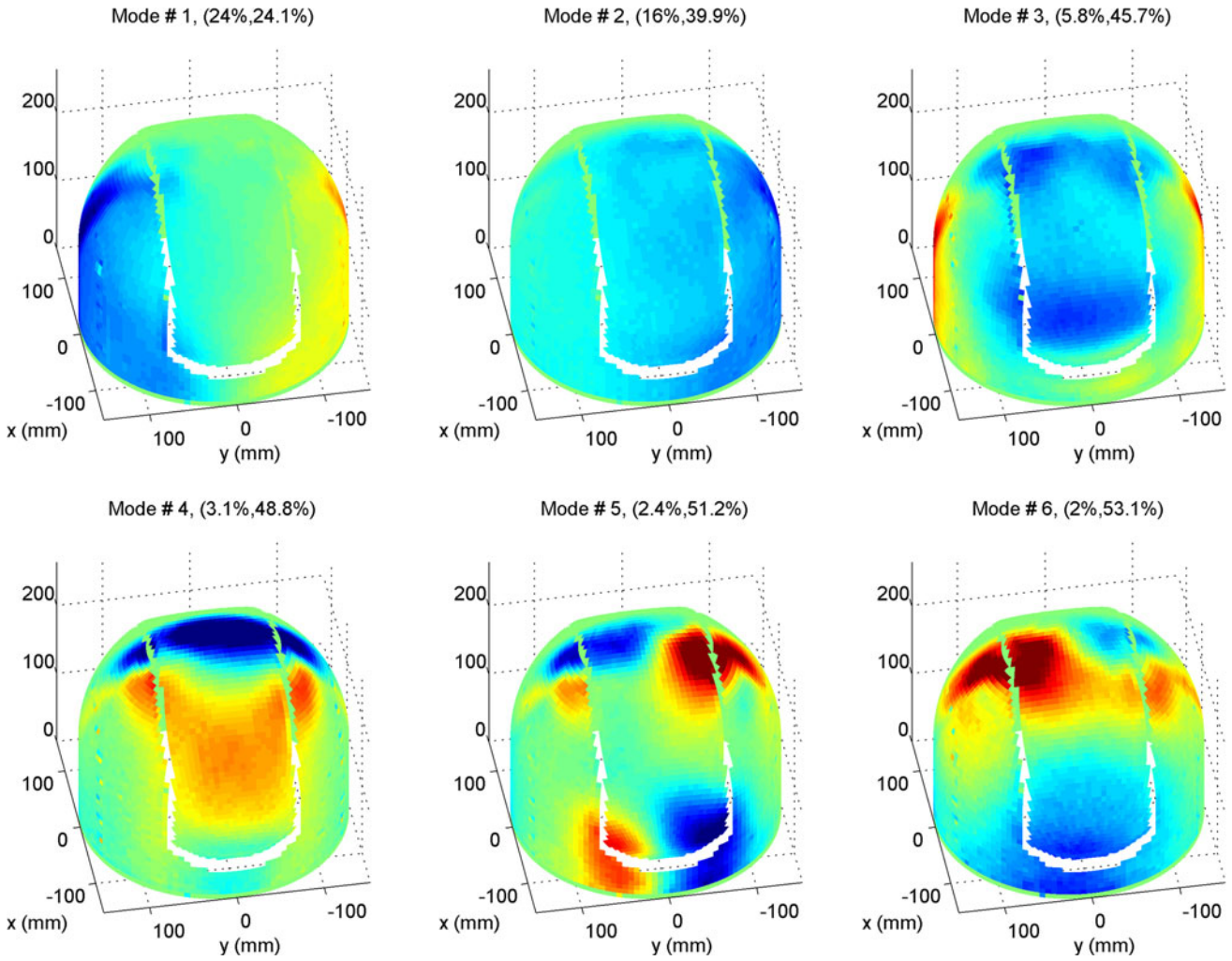

Fig. 25 First six joint POD modes for the (0, 45)-case. The corresponding normalized and the cumulative energies for each joint POD mode are given as a *first* and a *second number* in *parenthesis*. The flow goes along *x*-axis from *positive* to *negative* values. *Z*-axis is not labeled for clarity

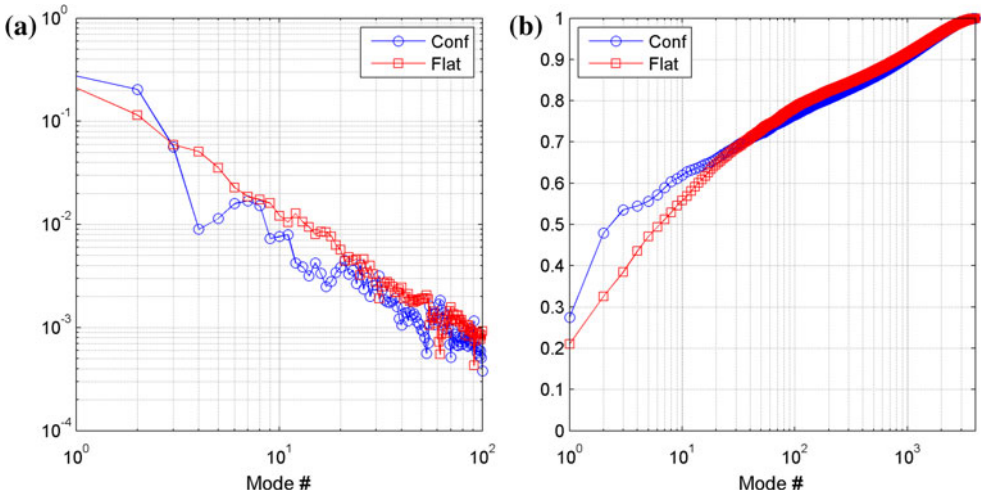

Fig. 26 **a** The individual normalized and **b** normalized cumulative mode energies for the conformal- and flat-window turrets for a joint set of POD modes for the (0, 45)-case

$M = 0.33$ on the surface of a hemisphere-on-cylinder turret with realistic surface features such as gaps and "smile" cutouts for both the conformal- and the flat-window apertures for different window azimuthal/elevation angles. Statistical quantities, such as surface maps of the time-averaged pressure standard deviations and instantaneous snapshots of pressure fields, were presented, compared and analyzed for different turret geometries. Additionally, POD was employed to analyze the topology and dynamics of the unsteady turbulent pressure structures for different turret geometries and window viewing angles.

The main sources of variation in the unsteady pressure on the turret were found to be the unsteady separation line and the separated recirculation region over the downstream portion of the turret. Different realistic surface features were also found to change the unsteady pressure field. The main contribution to these changes was from the "smiles." These large, cavity-like cutouts were found to significantly affect the instantaneous pressure field, depending on the "smiles" positions relative to the incoming flow. For the conformal-window turret with the window azimuthal angle of 0° or 180°, when "smiles" were located at the front and the back of the turret, the "smiles" effect was almost negligible, and the overall level of pressure fluctuations on the back surface of the turret was found to be minimal, the so-called baseline geometry. The maximum pressure fluctuations were found for the window azimuthal angle between 90° and 125°, when the "smiles" introduced additional strong vortical structures on either one or both sides of the turret downstream of the "smiles," significantly energizing the overall level of unsteady pressure fluctuations on the turret and changing the global dynamics of the separated region.

As the flow was able to travel through small gaps and to form weak jetlike flow through the gaps on the downstream potion of the turret, the gaps were found to locally introduce small vortical structures and to modify the instantaneous pressure field near the gaps. The slope discontinuity caused by the flat-window aperture also introduced additional localized vortical structures and related pressure fluctuations, when the window was faced either forward or sideways. Except facing forward, when the flat window tripped the incoming flow and introduced strong vortical structures on top of the turret, the presence of the flat window introduced local structures only and did not significantly change the overall unsteady pressure field.

POD analysis extracted dominant pressure modes and their temporal coefficients, allowing the study of different features of the unsteady pressure field for different turret geometries, window types and viewing angles. A joint POD analysis was introduced, which provides an alternative approach to compare relative contributions from a joint POD mode to unsteady pressure field for different geometries.

An additional benefit of the POD analysis was a significant noise reduction in the experimentally extracted pressure fields, providing well-spatially resolved pressure fields. Also, out of more than 4,000 computed POD modes, the first 100 POD modes were found to contain all essential information about the pressure field, thus providing a very efficient way to compress (by factor of 40) and store the data. It also shows that the POD technique is a very good complementary technique to PSP analysis, as it provides an efficient way to remove noise, to store and analyze the spatial–temporal pressure fields.

The joint POD analysis, although only briefly outlined in the paper for the sake of brevity, was shown to be an alternative powerful systematic way to compare pressure fields for different geometries. In general, the joint POD can be used to analyze massive spatial–temporal data as a function of some parameter(s), such as geometry, viewing angle and Reynolds number. For instance, it can be useful to quantify the effect of flow control by identifying modes mostly affected by the flow control.

Knowing the spatial distribution of POD modes, a temporal evolution of each mode can be estimated from a sparse unsteady pressure sensor array (Everson and Sirovich 1995) using an LSE approach (Adrian 1977; Bonnet et al. 1994). Also, the knowledge about the spatial distribution of POD modes provides strategies for optimal sensor placement to estimate a mode's temporal characteristics (Cohen et al. 2004). Thus, using a sparse unsteady sensor array, a temporal evolution of dominant pressure POD modes, and therefore the instantaneous pressure field, can be quickly estimated. The estimated pressure field can then be used, for instance, as a feedback signal to mitigate pressure-related effects around turrets, such as aeromechanical jitter or higher aero-optical modes (Burns et al. 2014).

In addition to providing a proper framework to study the time-resolved surface pressure field, POD modes can be useful to study aeroelastic response of the turret, as overall turret mechanical response can be found as a sum of responses to dominant uncorrelated POD modes. In De Lucca et al. (2013b), POD pressure modes were used to study unsteady forces acting on the turret for different turret geometries, and it was found that only the first five modes are needed to correctly predict the unsteady forces. So, a sparse unsteady pressure array can be properly placed using POD analysis to correctly measure (and potentially mitigate) unsteady forces acting on the turret.

The sensitivity of the surface unsteady pressure field to the realistic geometric features has to be taken into account when designing a turret, analyzing or predicting the aeromechanical jitter or when comparing the experimental results, typically performed using turrets with realistic features, and computational predictions, which usually use simplified hemisphere-on-cylinder-only turrets.

All presented measurements were taken at a relatively low Mach number of 0.33, and small transition effects for the flow around the turret were found to be present at this speed (Gordeyev and Jumper 2010; De Lucca et al. 2013b). Thus, in order to find Mach-number-independent POD modes, it is necessary to perform PSP experiments at a higher Mach number of at least 0.4. Also, the outlined approach to analyze the unsteady pressure fields can be highly useful at transonic speeds, where additional effects from a local unsteady shock on the dynamics of the separated flow from the turret are present (Gordeyev and Jumper 2010; Gordeyev et al. 2013).

Acknowledgments This work was funded by the Air Force Research Laboratory, Directed Energy Directorate and the High Energy Laser Division of the Joint Technology Office (HEL JTO) and supported by the Air Force Office of Scientific Research through Grant Number FA9550-07-1-0574. The US Government is authorized to reproduce and distribute reprints for governmental purposes notwithstanding any copyright notation thereon. The authors also wish to thank Dr. Jim Crafton of Innovative Scientific Solutions, Inc., for his many useful suggestions about the PSP technique.

References

Adrian RJ (1977) On the role of conditional averages in turbulence theory. In: Zakin J, Patterson G (eds) Proceedings of the fourth biennial symposium on turbulence in liquids. Science Press, Princeton, pp 323–332

Berkooz G, Holmes P, Lumley J (1993) The proper orthogonal decomposition in the analysis of turbulent flows. Annu Rev Fluid Mech 25(1):539–575

Bonnet JP, Cole DR, Delville J, Glauser MN, Ukeiley LS (1994) Stochastic estimation and proper orthogonal decomposition: complementary techniques for identifying structure. Exp Fluids 17:307–314

Burns R, Gordeyev S, Jumper EJ, Gogineni S, Paul M, Wittich DJ (2014) Estimation of aero-optical wavefronts using optical and non-optical measurements. AIAA paper 2014-0319

Carlbom I, Paciorek J (1978) Planar geometric projections and viewing transformations. ACM Comput Surv 10(4):465–502

Cohen K, Siegel S, Wetlesen D, Camero J, Sick A (2004) Effective sensor placements for the estimation of proper orthogonal decomposition mode coefficients in von Karman vortex street. J Vib Control 10(12):1857–1880

De Lucca N, Gordeyev S, Jumper EJ (2012) The study of aero-optical and mechanical jitter for flat window turrets. AIAA paper 2012-0623

De Lucca N, Gordeyev S, Jumper EJ (2013a) In-flight aero-optics of turrets. J Opt Eng 52(7):071405

De Lucca N, Gordeyev S, Jumper EJ, Hird K, Juliano TJ, Gregory JW, Thordahl J, Wittich DJ (2013b) The estimation of the unsteady force applied to a turret in flight. AIAA paper 2013-3136

Everson RM, Sirovich L (1995) The Karhunen–Loeve transform for incomplete data. J Opt Soc Am A 12(8):1657–1664

Fang S, Disotell KJ, Long SR, Gregory JW, Semmelmayer FC, Guyton RW (2011) Application of fast-responding pressure-sensitive paint to a hemispherical dome in unsteady transonic flow. Exp Fluids 50(6):1495–1505

Fang S, Long SR, Disotell KJ, Gregory JW, Semmelmayer FC, Guyton RW (2012) Comparison of unsteady pressure-sensitive paint measurement techniques. AIAA J 50(1):109–122

Gordeyev S, Jumper EJ (2010) Fluid dynamics and aero-optics of turrets. Prog Aerosp Sci 46:388–400

Gordeyev S, Post M, MacLaughlin T, Ceniceros J, Jumper EJ (2007) Aero-optical environment around a conformal-window turret. AIAA J 45(7):1514–1524

Gordeyev S, Cress J, Smith A, Jumper EJ (2010) Improvement in optical environment over turrets with flat window using passive flow control. AIAA paper 2010-4492

Gordeyev S, Burns R, Jumper EJ, Gogineni S, Paul M, Wittich DJ (2013) Aero-optical mitigation of shocks around turrets at transonic speeds using passive flow control. AIAA paper 2013-0717

Gregory JW, Asai K, Kameda M, Liu T, Sullivan JP (2008) A review of pressure-sensitive paint for high-speed and unsteady aerodynamics. Proc Inst Mech Eng Part G J Aerosp Eng 222(2):249–290

Gregory JW, Sakaue H, Liu T, Sullivan JP (2014) Fast pressure-sensitive paints for flow and acoustic diagnostics. Annu Rev Fluid Mech 46:303–330

Haralick RM (1980) Using perspective transformations in scene analysis. Comput Graph Image Process 13:191–221

Hird K, Juliano TJ, Gregory JW, De Lucca N, Gordeyev S, Jumper EJ, Thordahl J, Wittich DJ (2013) Study of unsteady surface pressure on a turret via pressure-sensitive paint. AIAA paper 2013-3135

Jelic R, Sherer S, Greendyke R (2013) Simulation of various turrets at subsonic and transonic flight conditions using overflow. J Aircr 50:398–409

Jumper EJ, Zenk M, Gordeyev S, Cavalieri D, Whiteley MR (2013) Airborne aero-optics laboratory. J Opt Eng 52(7):071408

Liu T, Sullivan JP (2005) Pressure and temperature sensitive paints. Springer, Berlin

Morgan PE, Visbal MR (2012a) Numerical simulation of flow over a submerged hemispherical flat-window turret. AIAA paper 2012-3042

Morgan PE, Visbal MR (2012b) Hybrid Reynolds-averaged Navier–Stokes/Large–Eddy simulation investigating control of flow over a turret. J Aircr 49(6):1700–1717

Morgan PE, White MD, Visbal MR (2011) Simulation of aero-optics for flow over a flat-window hemispherical turret. AIAA paper 2011-3264

Porter C, Gordeyev S, Zenk M, Jumper EJ (2013) Flight measurements of the aero-optical environment around a flat-windowed turret. AIAA J 51(6):1394–1403

Tan TN, Sullivan GD, Baker KD (1993) On computing the perspective transformation matrix and camera parameters. In: Proceedings of the 4th British machine vision conference, Surrey, England, pp 125–134

Vukasinovic B, Glezer A, Gordeyev S, Jumper EJ (2013) Flow control for aero-optics application. Exp Fluids 54:1492